Journal of Materials Chemistry C

ROYAL SOCIETY OF CHEMISTRY

PAPER

View Article Online
View Journal | View Issue

Cite this: J. Mater. Chem. C, 2024, 12, 15082

Orbital-engineered anomalous Hall conductivity in stable full Heusler compounds: a pathway to optimized spintronics†

Quynh Anh T. Nguyen,[a] Thi H. Ho,[bc] Seong-Gon Kim,[d] Ashwani Kumar[e] and Viet Q. Bui *[a]

Received 22nd May 2024,
Accepted 14th August 2024

DOI: 10.1039/d4tc02116a

rsc.li/materials-c

This comprehensive study leverages high-throughput density functional theory (DFT) to systematically explore the electronic, magnetic, and transport properties of 2904 full Heusler compounds, focusing on anomalous Hall conductivity (AHC). The investigation unveils a pronounced influence of the crystallographic phase and valence electron count on material stability and AHC. We report that Heusler compounds, particularly within the $L2_1$ phase and with 20 to 30 valence electrons, exhibit superior stability and AHC. Notably, Rh_2MnGa and Co_2MnAl emerge as exemplary, with AHCs of 1847 S cm^{-1} and 1646 S cm^{-1}, respectively, vastly outperforming traditional ferromagnets like Fe, Co, and Ni. The detailed electronic structure analysis of Co_2MnAl reveals a half-metallic character, crucial for high spin polarization and AHC, underscored by prominent Co–Co and Co–Mn hybridization. Furthermore, the study sheds light on the significant role of spin–orbit coupling in enhancing AHC through the modulation of band splitting and Berry curvature. The findings not only expand the understanding of Heusler compounds but also offer guidance in designing materials with tailored AHC for next-generation spintronic applications.

Introduction

Spintronics is an emerging field in information technology that combines three conventional information carriers: electron charge, spin, and photon.[1,2] These carriers represent the three important essential foundations of information technology: data processing with electron transport, data storage with an assembly of spins, and data transfer through optical connections. With the recent rapid advancements in information technology, there is a growing demand for both larger data-storage capacity and faster data processing. This can be achieved through the scaling of physical dimensions for enhanced speed, while maintaining power density by voltage scaling. Nevertheless, the optimization of these factors continues to be a difficult task.[3,4] This is because further reduction of the supply voltage could lead to an exponential increase in the leakage current. As a result, this not only negatively impacts the performance of the spintronic devices but also poses significant reliability issues.

Recent explorations into novel materials for fabricating next-generation electronic devices have attracted great attention.[3,5] Among the materials investigated, Heusler compounds are particularly notable in spintronics research due to their rich electronic and magnetic properties.[6–11] Full Heusler compounds are one of the main types of Heusler compounds. They have the chemical formula X_2YZ, where X and Y are transition metals and Z is an s–p element. With various possible combinations of X, Y and Z, the electronic structure and magnetic properties can be tuned as desired.[2] Recently, the application of full-Heusler compounds as multifunctional materials, including metals,[12] half-metals,[13] superconductors,[14] and topological insulators[15] with ferromagnetic and ferrimagnetic behaviors has been reported.[16,17] Furthermore, these compounds are renowned for their high Curie temperature[18,19] and substantial anomalous and spin Hall conductivity,[20,21] making them ideal for spintronic devices operating at room temperature.

The anomalous Hall effect (AHE) in ferromagnets has attracted considerable attention for investigations of electronic transport characteristics. This effect offers a straightforward way to examine the spin polarization of carriers, a crucial factor

[a] Advanced Institute of Science and Technology, The University of Danang, 41 Le Duan, Danang, Vietnam. E-mail: bqviet@ac.udn.vn, mrbuiquocviet@gmail.com
[b] Laboratory for Computational Physics, Institute for Computational Science and Artificial Intelligence, Van Lang University, Ho Chi Minh City, Vietnam
[c] Faculty of Mechanical – Electrical and Computer Engineering, School of Technology, Van Lang University, Ho Chi Minh City, Vietnam
[d] Department of Physics & Astronomy and Center for Computational Sciences, Mississippi State University, Mississippi State, Mississippi 39762, USA
[e] Max-Planck-Institut für Kohlenforschung, 45470 Mülheim an der Ruhr, Germany

† Electronic supplementary information (ESI) available: Detailed information on the complete database, which includes 2904 structures. See DOI: https://doi.org/10.1039/d4tc02116a

in the advancement of spintronic devices.[22,23] In half-metallic systems such as Heusler compounds, the AHE is very useful for probing spin–orbit coupling (SOC). This examination of SOC is crucial for understanding the influences of SOC on the evolution of the band structure and atomic order in relation to the growth parameters of the materials.[22] Karplus and Luttinger introduced the concept of anomalous velocity, which is understood as the curvature of the Berry phase in momentum space, providing a theoretical framework to explain the AHE in ferromagnetic materials.[24,25] Recently, the AHE has been extensively investigated in magnetic Heusler compounds through anomalous Hall conductivity (AHC).[20–22,26–30] Shubhankar Roy *et al.*[26] reported the essential role of spin–orbit coupling and its influence on the electronic band structure as well as the magnitude and direction of AHC. Yimin Ji *et al.*[21] performed high-throughput principles calculations to obtain the AHC of Heusler compounds, indicating the AHC is determined not just by the number of valence electrons or atomic weights, but rather by the specific characteristics of the electronic structures. Therefore, the AHC studies will reveal patterns and provide strategic insights for engineering materials with tailored properties for spintronic applications.

Herein, we employed high-throughput density functional theory (DFT) calculations to explore and predict the AHE of 2904 full-Heusler compounds. Our work has identified compounds with remarkable AHC values, such as Rh_2MnGa, which exhibits an AHC of 1847 S cm^{-1} and a magnetic moment of $4.07\mu_B$, highlighting its exceptional stability and potential for spintronic applications. Similarly, Co_2MnAl with an AHC of 1646 S cm^{-1} and a robust magnetic moment of $4.14\mu_B$, along with Ti_2PtSn and Mn_2TiAl with significant AHCs of 1319 and 1267 S cm^{-1}, respectively, showcases the versatility of Heusler compounds for technological applications. This extensive dataset spans a broad spectrum of elemental substitutions within the Heusler structure, facilitating a systematic assessment of how compositional variations influence the AHE. Our approach not only encompasses the calculations of AHC but also delves into the detailed investigation of the electronic structures and magnetic stability of these compounds.

The relevance of this study lies in the unveiling of novel Heusler compounds with significant AHE potential, poised to play a vital role in the advancement of next-generation spintronic devices. By comprehensively understanding the interplay between the electronic structure and AHE, we are paving the way for the development of materials with tailored properties, optimal for specific applications in magnetic storage and spin-based electronics. The findings from our work significantly contribute to the growing database of Heusler compounds with characterized electronic and magnetic properties, thereby propelling further research and technological innovations in the dynamic field of spintronics.

Computational details

Our computational investigation into the electronic structures and AHC of full-Heusler compounds utilizes the spin-polarized density functional theory as implemented in the Vienna *Ab initio* Simulation Package (VASP).[31–33] Within this framework, the projector augmented-wave (PAW) method serves as the foundation for our calculations.[34] The exchange–correlation effects are approximated by generalized gradient approximation (GGA), precisely following the Perdew–Burke–Ernzerhof (PBE) formalism,[35] which has been rigorously tested for the reliable portrayal of electronic properties in a diverse array of materials. A careful selection of computational parameters ensures the accuracy of our results: we employ an energy cutoff of 400 eV for plane-wave basis set expansion to guarantee the precise representation of electronic wavefunctions. Brillouin zone sampling is accomplished with a dense Monkhorst–Pack k-mesh of $15 \times 15 \times 15$, chosen to strike a balance between computational efficiency and the resolution necessary for accurate electronic structure determination. The convergence of energy between successive self-consistent field iterations is stringently controlled to within 10^{-6} eV, ensuring that the calculated properties reflect a true ground state. Further delving into the electronic structure, we construct maximally localized Wannier functions (MLWFs) from the computed Bloch states *via* the Wannier90 package.[36] This approach facilitates the quantification of the intrinsic contributions to AHC, enabling us to dissect the complex interplay between band topology and transport phenomena in these compounds.

For each configuration of Heusler compounds, our computational strategy involves generating 18 maximally localized Wannier functions (MLWFs) for the transition metal atoms X and Y, and 8 MLWFs for the Z atom from the Bloch states. This is approximately twice the number of MLWFs generally utilized, chosen to enhance the precision of our electronic structure representation. The initial projections of the Bloch states for X and Y atoms are chosen as a hybridization of s, p, and d orbitals, specifically sp^3d^2, and for Z atoms as sp^3. To ensure the accurate disentanglement of bands and generation of MLWFs, the upper limit of the energy window is set to 5.0 eV above the Fermi level (E_F). For the construction of the MLWFs, we employed a dense k-mesh of $4 \times 4 \times 4$.

The intrinsic contribution to anomalous Hall conductivity (AHC) is quantified through the Kubo formula, which is mathematically expressed as follows:[37]

$$\sigma_{xy}^{z} = \frac{e}{\hbar}\int \frac{d^3k}{(2\pi)^3}\sum_n f_{kn}\Omega_{n,xy}^{z}(k) \quad (1)$$

$$\Omega_{xy}^{z}(k) = -\sum_{n\neq m} 2\mathrm{Im}\frac{\langle kn|v_x|km\rangle\langle km|v_y|kn\rangle}{(E_{kn}-E_{km})^2} \quad (2)$$

where $\Omega_{xy}^{z}(k)$ is the Berry curvature, f_{kn} is the Fermi–Dirac distribution function, $|kn\rangle$ and E_{kn} are the Bloch state and energy for the n-th state, and v_x and v_y are the velocity operators. A k-mesh of $100 \times 100 \times 100$ was used to achieve the numerical convergence for AHC calculations.

By applying these rigorous computational techniques, we ensure a comprehensive understanding of the dependency of the AHC on the electronic structure, which is crucial for

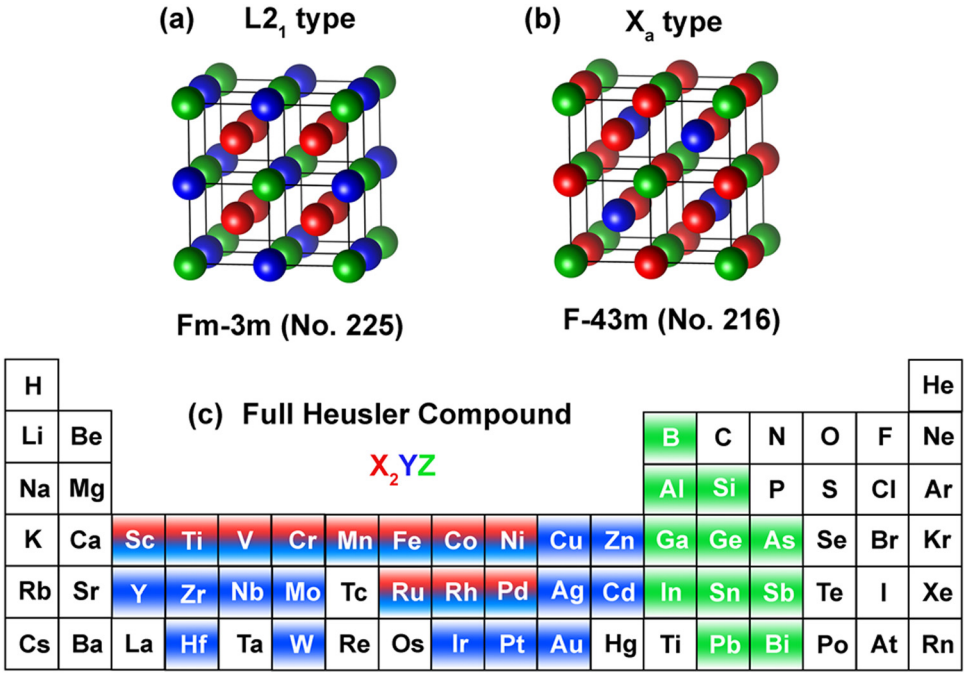

Fig. 1 The structure of (a) a regular Heusler compound, X_2YZ and (b) an inverse Heusler compound, XYXZ, where X occupies the 8c ($\frac{1}{4}$, $\frac{1}{4}$, $\frac{1}{4}$) Wyckoff position, Y occupies the 4b ($\frac{1}{2}$, $\frac{1}{2}$, $\frac{1}{2}$) Wyckoff position, and Z occupies the 4a (0,0,0) Wyckoff position. (c) Periodic table, where the color of the atoms corresponds to the colors of X, Y, and Z.

tailoring materials to meet the specific needs of spintronic technology.

For the structural construction of the full cubic Heusler compounds under consideration, we focused on the two most prevalent crystallographic phases: the regular $L2_1$ and the inverse X_a. The $L2_1$ phase, illustrated in Fig. 1(a), is characterized by cubic symmetry within the space group $Fm\bar{3}m$ (SG 225), where transition metals occupy the X and Y positions (depicted in blue and green, respectively) and the main group elements are denoted by Z (illustrated in red). In this configuration, the X atoms are positioned at the 8c Wyckoff sites ($\frac{1}{4}$, $\frac{1}{4}$, $\frac{1}{4}$), Y atoms at the 4b sites ($\frac{1}{2}$, $\frac{1}{2}$, $\frac{1}{2}$), and Z atoms at the 4a sites (0, 0, 0). Conversely, the inverse X_a structure, shown in Fig. 1(b) and associated with the space group $F\bar{4}3m$ (SG 216), presents a unique arrangement where the X transition-metal atoms have a lower valence compared to the Y transition-metal atoms.

The exploration comprised 2904 potential structures, each derived from a diverse palette of elements occupying the X, Y, and Z positions as delineated in the periodic table of Fig. 1(c). For geometrical optimization, we fully relaxed the unit cells, permitting atomic positions to be refined until reaching an energy convergence threshold of less than 10^{-5} eV for the optimization steps. This meticulous optimization process ensures that the computed properties are reflective of the lowest energy structures, a prerequisite for accurate predictions of physical behaviors such as AHC and magnetic stability.

Formation energy is used to explore the structural stability of Heusler compounds, calculated using the following formula:

$$\Delta F[X_2YZ] = \frac{1}{4}(E[X_2YZ] - 2E[X] - E[Y] - E[Z]), \qquad (3)$$

where $E[X_2YZ]$, $E[X]$, $E[Y]$, and $E[Z]$are the total energies per atom in the bulk form of X_2YZ, X, Y, and Z, respectively.

Results and discussion

In this study, we have conducted a thorough investigation of the stability and electronic structures across an expansive set of 2904 full Heusler compounds, with an aim to deepen the understanding of their potential in advanced applications. Fig. 2 illustrates the initial segment of our findings, portraying the intricate energy profiles that dictate the phase stability and hence the usability of these materials within nanotechnological domains, such as spintronics. In Fig. 2(a), the energy difference as a function of the total number of total valence electrons (Ne) between the $L2_1$ and X_a structures is elucidated; negative values indicate that the X_a structure is energetically more favorable, whereas positive values denote a predominance of the $L2_1$ structure, especially notable as Ne increases. Aggregation according to Ne in Fig. 2(c) reveals a distinct peak at Ne equal to 25, within a range concentrated between 20 and 30 Ne, indicating a marked preference for the stability of $L2_1$ structures in this electronic configuration. The X_a structures exhibit a more even distribution, suggesting a less pronounced dependency on Ne. Fig. 2(b) presents the formation energies, with negative values signifying stability, dominating the assembly of compounds; this stability profile is reflected in Fig. 2(d), which, when compiled by Ne, displays a trend analogous to the $L2_1$ and X_a structural distribution. The analysis delineates that Heusler compounds exhibit a predilection for stability within the $L2_1$ phase, particularly for combinations of X, Y, and Z resulting in

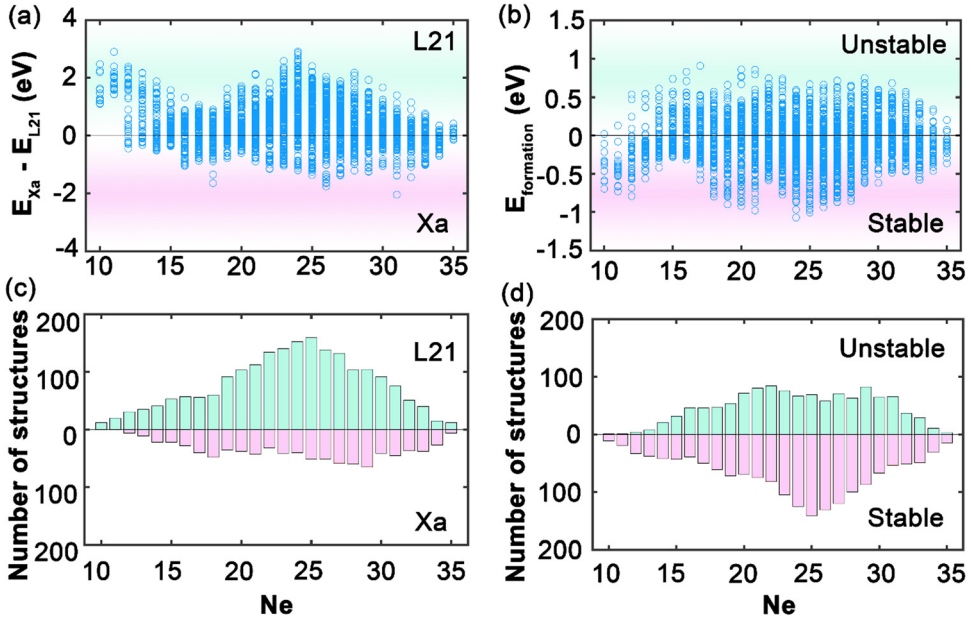

Fig. 2 (a) Energy difference as function of total valence electron Ne between $L2_1$ and X_a structure and (b) formation energy for all structures. Number of structures as a function of Ne for (c) $L2_1$ and X_a structures and (d) unstable and stable structures.

a total Ne within the 20–30 range. This not only identifies a domain of structural stability but also highlights an optimal region for engineering materials with the desired electronic configurations for spintronic applications, laying a vital foundation for the development of materials with properties tailored for the progression of advanced technological applications.

Fig. 3 illustrates the AHC as a function of the total valence electron Ne in full Heusler compounds. This behavior is categorized into three distinctive regions which correlate closely with the Slater–Pauling rule[38,39] for total magnetic moment: $10 \leq Ne \leq 16$, $16 \leq Ne \leq 25$, and $Ne \geq 25$. Such correlation suggests that AHC is intimately linked with the magnetic properties of these materials, adhering to the foundational magnetic behavior predicted using the Slater–Pauling curve. The first region, where $10 \leq Ne \leq 16$, is characterized by a progressive increase in AHC, peaking sharply at Ne = 14. Here, we observe the highest AHC values corresponding to compounds with X constituents such as Sc and Ti. This suggests that, in this range, the compounds with early transition metals are more likely to exhibit enhanced Hall conductivity, which can be attributed to their lower d-band occupancy allowing for a higher degree of spin polarization as per the Slater–Pauling curve. In the intermediate region of $16 \leq Ne \leq 25$, AHC demonstrates a similar pattern, climbing to its apex at Ne = 21, then gradually declining. The compounds yielding high AHC in this segment predominantly have X constituents like Mn and Fe. This can be rationalized by considering the increased d-band filling for these elements, leading to more complex band interactions and potentially higher magnetic moments that favor substantial AHC values as they approach the saturation of the d-band just before Ne reaches 24. The final region, $Ne \geq 25$, where AHC is shown to be maximal at Ne = 28, corresponds to elements with X constituents like Fe, Ru, Co, and Rh. The high AHC values in this range could be linked to the closeness to full d-band occupancy, which would be expected to reduce the magnetic moment as per the Slater–Pauling behavior. These trends across the different regions reflect the Slater–Pauling behavior where the AHC intensifies, reaches a maximum, and then tapers, mirroring the corresponding magnetic phenomena. The pronounced peaks in AHC within specific Ne ranges suggest that optimal electronic structures exist for maximizing Hall conductivity. This insight opens avenues for strategically engineering Heusler compounds with enhanced magnetic and electronic transport properties, tailored for spintronic applications. The data thus provide a roadmap for the compositional tuning of Heusler compounds to harness their full potential in advanced technological applications, particularly in devices that leverage spintronic phenomena.

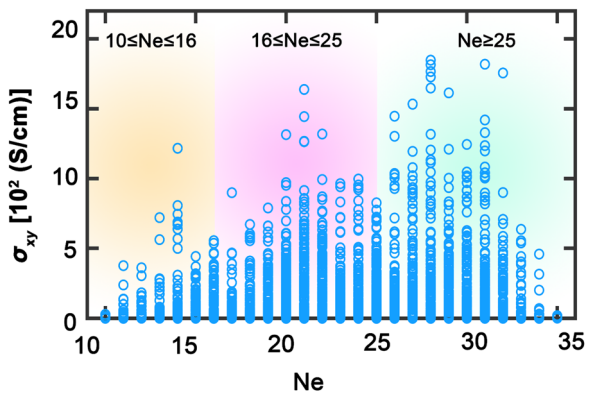

Fig. 3 Anomalous Hall conductivity σ_{xy} as a function of total valence electron Ne. Yellow, purple, and cyan backgrounds distinguish three areas: $10 \leq Ne \leq 16$, $16 \leq Ne \leq 25$, and $Ne \geq 25$, respectively.

Additionally, Table 1 elucidates the remarkable magnitude of AHC within an array of Heusler compounds, juxtaposed against their stability and magnetic characteristics. Our

calculated ΔF shows good agreement with the open quantum materials dataset.[40] All cases show positive hull distance ΔH, except for Rh_2MnAl with $\Delta H = 0$, which means that the material is thermodynamically stable. This reveals that select compounds, notably Rh_2MnGa and Co_2MnAl, exhibit not only formidable stability, indicated by their negative formation energies, but also AHC values of 1847 and 1646 S cm^{-1}, respectively. These figures significantly surpass traditional AHCs of elemental ferromagnets such as Fe, Co, and Ni.[41–43] Overall, our calculated AHC exhibits similar tendency and order of magnitude to previously reported values, especially with $19 \leq Ne \leq 33$.[44] The observed increase in the AHC is directly linked to the distinctive electronic structure of Heusler compounds. Their adaptive alloying capability enables extensive modulation of magnetic and transport properties. A deliberate selection of elements X, Y, and Z leads to electronic configurations that yield high magnetic moments, which in turn is manifest in elevated AHC values. This correlation underscores the profound impact of targeted elemental synthesis on the emergent physical properties of these compounds, as demonstrated in our findings. The data clearly show that enhancements in AHC result from strategic element selection within the Heusler framework, a crucial factor for achieving exceptional AHC. This is vital for advancing spintronics, particularly in applications that require precise spin current detection and efficient magnetic switching.

To explore this further, we performed a detailed correlation analysis between AHC and the total magnetic moment (M_{tot}) for the compounds listed in Table 1, observing a moderately strong linear correlation with an R^2 value of 0.663 (Fig. S1(a), ESI†). However, extending this analysis to the entire database reveals a more complex relationship, with a wide range of AHC values for the same M_{tot}, as shown in Fig. S1(b) (ESI†). Thus, this complexity necessitates considering additional factors such as the total valence electron count (Ne), which follows the Slater–Pauling rule. Indeed, plots of AHC and M_{tot} as a function of Ne (Fig. S1(c) and (d), ESI†) reveal similar behavior, delineating three regions: $10 \leq Ne \leq 16$, $16 \leq Ne \leq 25$, and $Ne \geq 25$. Additionally, we have calculated the spin polarization for each of the full Heusler compounds listed in Table 1 using the formula $P = \frac{N_\uparrow - N_\downarrow}{N_\uparrow + N_\downarrow}$, where $N_\uparrow$ and $N_\downarrow$ are the densities of states for the up and down spin channels, respectively. The spin polarization values, which range from 17% to 97%, highlight the significant variation in electronic configurations across different compounds (Fig. S2, ESI†). High spin polarization indicates a high degree of spin polarization at the E_F, which is beneficial for spintronic applications. To facilitate comparison, we have included additional theoretical and experimental data in Table 1. The Co_2YZ Heusler compounds have been extensively studied both theoretically and experimentally due to their outstanding reputation in the field. Consequently, we have also provided the properties of the Co_2MnZ family in Table S1 (ESI†). Our calculated values for the M_{tot} and P align closely with other computational and experimental results.

To further explore the factors influencing the AHC in Heusler compounds, we analyzed the relationship between AHC and the valence electron, as well as the electronegativity differences between the constituent elements. Fig. S3 (ESI†) presents the AHC as a function of the valence electrons for X, Y, and Z elements and the valence electron differences between

Table 1 The largest anomalous Hall conductivity ($|\sigma_{xy}|$) alongside the stability and magnetic characteristics for the stable compounds within each X_2YZ family. The table lists the stable phase, formation energy (ΔF in eV per atom), Hull distance (ΔH in eV per atom), $|\sigma_{xy}|$ (S cm^{-1}), total magnetic moment (M_{tot} in μ_B), spin polarization (P in %), and the anomalous Nernst conductivity ($|\alpha_{xy}|$ in A K^{-1} T^{-1}) at T = 300 K. The data illustrate the correlation between the stability, electronic configuration, and magnetic properties with the AHC for different Heusler compounds

X_2YZ	Stable phase	ΔF (eV per atom)	ΔH (eV per atom)	$\lvert\sigma_{xy}\rvert$ (S cm^{-1})	M_{tot} (μ_B)	P (%)	$\lvert\alpha_{xy}\rvert$ (A K^{-1} T^{-1})
Rh_2MnGa	$l2_1$	−0.569 −0.537[a]	0.000[a]	1847 1862[b]	4.07 4.10[b] 4.05[c]	93	1.55 3.82[b]
Co_2MnAl	$l2_1$	−0.385 −0.356[a]	0.009[a]	1646 1631[b] 1600[d]	4.14 4.04[b] 4.01[e]	63 68[f] 75[g]	2.62 1.93[b]
Ti_2PtSn	$l2_1$	−0.429 −0.487[a]	0.260[a]	1319	1.79	48	3.29
Mn_2TiAl	$l2_1$	−0.397 −0.344[a]	0.002[a]	1267 1128[b]	3.01 2.98[h]	81 82[h]	1.81 1.03[b]
Ru_2WSi	$l2_1$	−0.020 −0.03[a]	0.308[a]	1036	1.24	34	2.99
Sc_2CrSb	$l2_1$	−0.167 −0.167[a]	0.422[a]	899	2.88 3.16[i]	17	4.68
V_2IrAl	x_a	−0.480 −0.472[a]	0.093[a]	869	1.60	70	2.29
Cr_2IrGe	x_a	−0.067 −0.072[a]	0.138[a]	826	0.97	97	0.04
Fe_2MnGa	l21	−0.024 −0.014[a]	0.042[a]	717 454[b]	2.14 2.02[j]	66 74[j]	5.85
Ni_2RhAl	x_a	−0.408 −0.425[a]	0.124[a]	513	0.84	75	5.54

[a] Theoretical data.[40] [b] Theoretical data.[44] [c] Theoretical data.[46] [d] Experimental data.[47] [e] Experimental data.[45] [f] Theoretical data.[48] [g] Theoretical data.[49] [h] Theoretical data.[50] [i] Theoretical data.[51] [j] Theoretical data.[52]

them. ΔXY, ΔXZ, and ΔYZ denote valence electron differences between X and Y, X and Z, and Y and Z, respectively. The largest AHC values for X elements occur at valence electrons of 7 and 9, while for Y elements, the highest AHC is observed at 7, 9, and 10 valence electrons. For Z elements, the distribution of AHC is relatively uniform across different valence electrons. Additionally, Fig. S3 (ESI†) shows that significant AHC values for ΔXY are observed in the ranges $-2 \leq \Delta XY \leq 0$ and $\Delta XY \approx 2$, for ΔXZ at 4 and 6, and for ΔYZ at 4, 6, and 7. Furthermore, Fig. S4 (ESI†) shows the AHC as a function of electronegativity for X, Y, and Z elements and the electronegativity differences between them (ΔXY, ΔXZ, ΔYZ). These analyses reveal that both valence electron and electronegativity differences play crucial roles in determining the AHC. For instance, the highest AHC values are observed for X elements with electronegativity values of approximately 1.8 and 2.3, for Y elements at around 1.6 and 2.2, and for Z elements uniformly across the studied range. The differences in electronegativity that yield high AHC values are concentrated around −0.4, 0, and 0.7 for ΔXZ, and $-0.4 \leq \Delta XZ \leq 0.7$. Furthermore, high AHC values are observed around $-0.3 \leq \Delta YZ \leq -0.1$, and $\Delta YZ \approx -0.5$ and 0.5. These results highlight the importance of considering both the valence electron count and electronegativity in the design of Heusler compounds with optimized AHC properties.

We also provide the anomalous Nernst conductivity (ANC), closely related to the anomalous Hall effect, is a phenomenon in which a current is induced by a temperature gradient. In this study, we calculated the ANC using the formula[53] $\alpha_{xy} = \frac{\pi^2 k_B^2 T}{3e}\frac{\partial \sigma_{xy}}{\partial \varepsilon}$, where k_B is the Boltzmann constant, T is the temperature, and $\partial\varepsilon = 0.01$ eV is the energy interval. Fig. S5 (ESI†) shows ANC as a function of chemical potential μ for selected compounds: Rh_2MnGa, Co_2MnAl, Ti_2PtSn, Mn_2TiAl, Ru_2WSi, Sc_2CrSb, V_2IrAl, Cr_2IrGe, Fe_2MnGa, and Ni_2RhAl. ANC exhibits significant sensitivity to variations in the E_F, similar to AHC. For instance, in Mn_2TiAl and Fe_2MnGa, a high slope of AHC near E_F results in a pronounced ANC. As the temperature increases, ANC also increases, highlighting the interplay between thermal effects and the electronic structure. The specific values of ANC at E_F for T = 300 K are included in Table 1.

Fig. 4 presents a nuanced view of AHC across Heusler compounds, categorized by the transition metal element X when X is less than half-filled. It is evident that the distribution of AHC largely skews toward Ne values less than 25, with the notable exception of Mn-based compounds, reflecting a strong dependence on the specific electronic configuration of the transition metal element. For Sc-based compounds, the highest AHC is observed at Ne = 14, which is suggestive of the fewer d-electrons in Sc facilitating higher spin polarization and resultant Hall conductivity. Ti compounds follow a distinct pattern, peaking at Ne = 22, which may reflect the more complex d-orbital interactions as Ti approaches half-filling. The high AHC for Mn at Ne = 21 underscores its robust magnetic character among the transition metals, likely contributing to its pronounced Hall effect. Notably, the AHC for V- and Cr-containing compounds remains relatively consistent across the studied Ne range, possibly indicating a more stable electronic structure that is less sensitive to the variation in the number of valence electrons. The relatively lower AHC values for these elements compared to Sc and Ti suggest that their closer proximity to half-filling results in less pronounced spin polarization effects conducive to AHC. As a half-filled transition metal, Mn demonstrates larger AHC values affirming the strong link between magnetic properties and AHC. This correlation is consistent with the established understanding that magnetic moments and spin–orbit coupling are significant

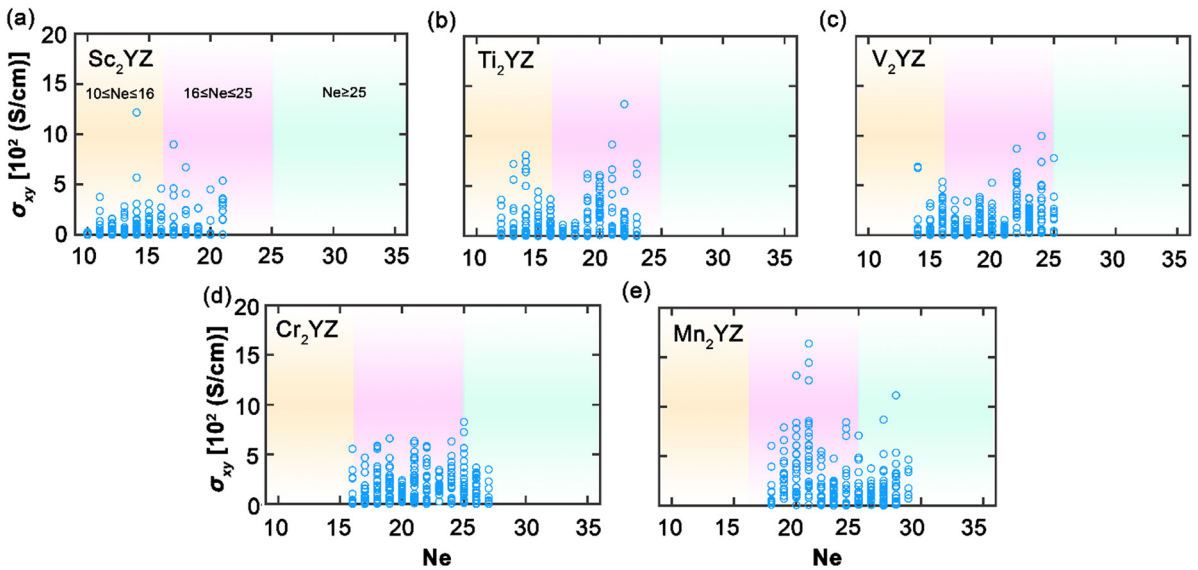

Fig. 4 Anomalous Hall conductivity σ_{xy} as a function of total valence electron Ne for (a) Sc_2YZ, (b) Ti_2YZ, (c) V_2YZ, (d) Cr_2YZ, and (e) Mn_2YZ, where X is a less than half-filled transition metal. Yellow, purple, and cyan backgrounds distinguish three areas: $10 \leq Ne \leq 16$, $16 \leq Ne \leq 25$, and $Ne \geq 25$, respectively.

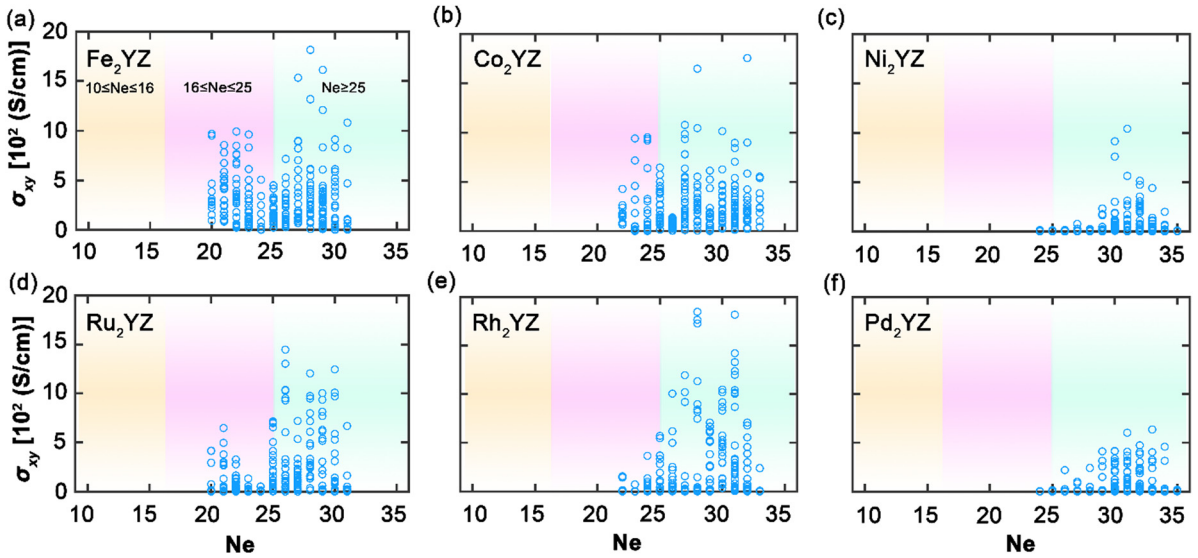

Fig. 5 Anomalous Hall conductivity σ_{xy} as a function of total valence electron Ne for (a) Fe_2YZ, (b) Co_2YZ, (c) Ni_2YZ, (d) Ru_2YZ, (e) Rh_2YZ, and (f) Pd_2YZ, where X is a more than half-filled transition metal. Yellow, purple, and cyan backgrounds distinguish three areas: $10 \leq Ne \leq 16$, $16 \leq Ne \leq 25$, and $Ne \geq 25$, respectively.

contributors to AHC in such materials. The data from Fig. 4, therefore, not only provide insight into the electronic structure-dependent behavior of AHC in Heusler compounds but also point to the potential of specific elemental configurations, particularly those involving Mn, in achieving high AHC values suitable for spintronic applications.

Extending our analysis to Fig. 5, we examine the distribution of AHC for Heusler compounds where X element is more than half-filled. The data primarily cover Ne values greater than 20, indicating that these compounds generally exhibit higher AHCs compared to those with X elements that are less than half-filled, as shown in Fig. 4. The AHC values within this group, particularly for Fe-, Co-, Ru-, and Rh-based compounds, are notably higher, which is in line with their position in the periodic table, alluding to their similar valence electron counts. This similarity results in comparable electronic structures that facilitate high AHC, with the largest values for Fe appearing between Ne values of 27 and 29 and for Co at Ne = 22, likely due to their proximity to full d-band occupancy which promotes enhanced spin polarization. In contrast, Ni and Pd, both near or at full d-band filling, show reduced AHC values. The diminished AHC can be attributed to poorer d-orbital hybridization, as full filling leads to a lower number of available states for conduction, thus reducing the probability of spin-dependent scattering essential for a large AHC. This trend is particularly interesting as it reflects the sensitivity of AHC to the specific electronic configuration and hybridization of d-orbitals in Heusler compounds. The insights obtained here underscore the nuanced interplay between electron filling, magnetic properties, and resultant AHC. Understanding this relationship is vital for the tailored design of Heusler compounds with high AHC for spintronic applications, where maximizing spin-dependent transport phenomena is crucial.

Delving deeper into the electronic structure, Fig. 6 presents the band structures for Co_2MnAl, segregated into spin-up and spin-down channels, which sheds light on the intrinsic properties leading to its high AHC. This compound, which is ferromagnetic, aligns with the Slater–Pauling rule manifesting a total magnetic moment close to $4\mu_B$, with individual contributions of $0.77\mu_B$ from Co and $2.7\mu_B$ from Mn for a total valence electron count of 28. Our results show good agreement with previous studies.[44,45] The band structure of Co_2MnAl reveals a half-metallic character, with the spin-up channel exhibiting metallic behavior, with bands almost fully occupied near the E_F. Conversely, the spin-down channel acts as a semiconductor, displaying a direct gap at the Γ point of 0.46 eV. This gap is pivotal as it suggests high spin polarization at E_F, which is a desirable trait for spintronic applications due to its potential to facilitate spin current without charge current. The contribution of Al to AHC is negligible since its states are distributed far from E_F. In contrast, the states of Co are closer to E_F, with smaller exchange splitting compared to Mn, implying that the contribution of Co to the total AHC is less than that of Mn. At the Γ point, hybridization between the states of Co leads to a bandgap opening, further illustrating the complex interaction

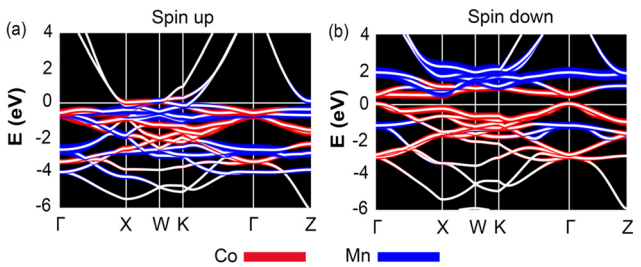

Fig. 6 Band structure of Co_2MnAl for (a) spin-up and (b) spin-down channels. Red and blue denote the contributions of Co and Mn, respectively.

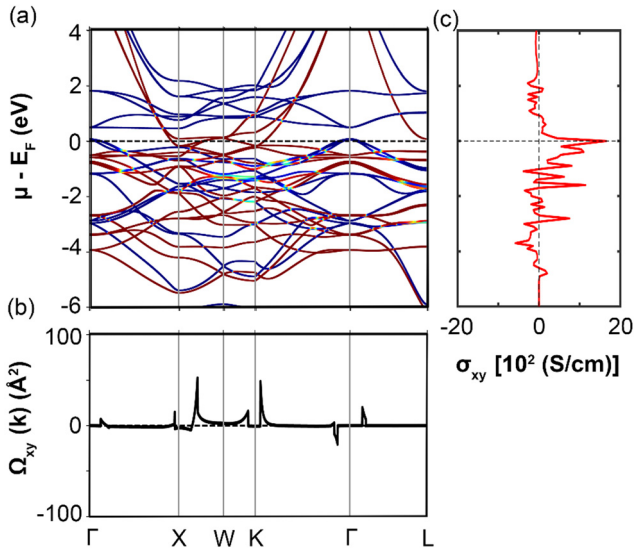

Fig. 7 (a) Band structures along the high-symmetry lines and (b) Berry curvature along the same path of Co_2MnAl. Colors represent $\langle S_Z \rangle$. (c) AHC as a function of chemical potential μ. The Fermi energy E_F is set to zero.

between elements and the collective impact on the electronic properties of the material. Analyzing this band structure is fundamental in understanding the underlying mechanisms that govern the AHC in Co_2MnAl. It is the intricate hybridization of the Co and Mn states and the resultant energy band dispersion that underpins the substantial AHC observed. The calculations performed for Co_2MnAl not only confirm its high AHC but also provide a concrete example of how electronic band structure details are paramount in evaluating and predicting material properties for advanced spintronic devices.

Fig. 7 provides a compelling visualization of the band structure and Berry curvature for Co_2MnAl, a ferromagnetic Heusler compound, in both spin channels after including the SOC. The bands are color-coded from blue (representing spin $-\hbar/2$) to red (representing spin $+\hbar/2$), clearly indicating that most bands are well split by S_Z, highlighting the significant influence of SOC. The band structure (Fig. 7a) exhibits the profound effect of SOC, as spin is not a good quantum number in its presence, leading to bands that are non-degenerate in most parts of the k-space. The band splitting, which is particularly evident along high-symmetry lines, is a key factor in determining the AHC of the material. In Fig. 7b, the total Berry curvature Ω_{xy} along the same high-symmetry lines reflects a general prevalence of $\Omega > 0$ over $\Omega < 0$, contributing to a sizeable total AHC of 1646 S cm^{-1}, which is in good agreement with both experimental and theoretical reports.[44,46] Notably, the distribution of the Berry curvature shows two dominant positive peaks at 1/3XW and near K, while smaller peaks appear along GX, WK, and FZ. The negative Berry curvature is less prevalent, with a single significant peak along KG. The AHC as a function of chemical potential μ (Fig. 7c), within the same energy range as the band structure, peaks at the E_F. This maximum in AHC corresponds to the maximal spin polarization between the spin-up and spin-down channels and is predominantly contributed by the Co–Co hybridization. The spectrum of this large peak in AHC ranges from approximately −0.8 to 1 eV, indicating that the regions of high Co–Co and Co–Mn hybridization contribute significantly to AHC. Outside this energy range, the AHC values diminish. The detailed analysis of Fig. 7 hence underlines the critical role of SOC and the resultant band splitting in enhancing the AHC in Co_2MnAl. These insights into the spin-resolved electronic structure and the distribution of the Berry curvature across the Brillouin zone are essential for understanding the mechanisms driving the high AHC in this compound, affirming its suitability for spintronic applications where high spin-polarization and efficient spin-current generation and manipulation are desired.

Conclusion

In conclusion, this extensive study on full Heusler compounds using high-throughput DFT calculations has uncovered remarkable insights into their electronic, magnetic, and transport properties, particularly their AHC. Our systematic investigation into over 2904 compounds has revealed that both the crystal structure and the electron count play critical roles in determining the stability and the AHC of these materials. Key findings from our research highlight that Heusler compounds with a total valence electron count (Ne) between 20 and 30 exhibit enhanced stability within the $L2_1$ phase, as evidenced by compounds such as Rh_2MnGa, which demonstrates an AHC of 1847 S cm^{-1} and a magnetic moment of 4.07μ_B, and Co_2MnAl, with an AHC of 1646 S cm^{-1} and a magnetic moment of 4.14μ_B. These values are notably superior to those of elemental ferromagnets like Fe, Co, and Ni, underscoring the potential of Heusler compounds in transcending the performance of conventional magnetic materials.

Our focused examination of Co_2MnAl revealed a half-metallic nature, which is instrumental in achieving high spin polarization and, consequently, a high AHC. The intricate interplay between Co–Co and Co–Mn hybridization within this specific compound has been shown to contribute significantly to the observed AHC, which peaks in the vicinity of the Fermi level. Moreover, the study elucidates the crucial role of SOC in the band structure of Heusler compounds. SOC not only influences band splitting but also substantially affects the Berry curvature distribution, which directly impacts AHC. The presented results not only contribute to the fundamental understanding of the intrinsic properties of Heusler compounds but also serve as a guide for the design of new materials with high AHC for advanced spintronic applications. By delineating the correlation between AHC and the intrinsic magnetic and electronic properties of the materials, we pave the way for the strategic synthesis of Heusler compounds with customized properties for specific technological applications.

Our research thus concludes with significant implications for the field of spintronics, providing a solid foundation for the future exploration of novel magnetic materials with high AHC, targeting applications that range from spin current detection to magnetic switching in state-of-the-art devices.

Author contributions

Viet Q. Bui supervised the research and wrote the original manuscript. Quynh Anh T. Nguyen and Thi H. Ho performed the DFT calculations. All authors participated in revising the manuscript.

Data availability

The data supporting the findings of this study are available within the article and the ESI.† Additional data, including computational codes and raw data files generated during the study, are available from the corresponding author upon reasonable request.

Conflicts of interest

The authors declare no conflicts of interest.

Acknowledgements

This work was financially supported by the Vietnam Ministry of Education and Training (code: B2023.DNA.11). We also thank the US DOE INCITE program and National Science Foundation ACCESS program for providing the computing resources.

References

1 A. Hirohata and K. Takanashi, *J. Phys. D: Appl. Phys.*, 2014, **47**, 193001.
2 P. Barla, V. K. Joshi and S. Bhat, *J. Comput. Electron.*, 2021, **20**, 805–837.
3 E. C. Ahn, *npj 2D Mater. Appl.*, 2020, **4**, 17.
4 B. Dieny, I. L. Prejbeanu, K. Garello, P. Gambardella, P. Freitas, R. Lehndorff, W. Raberg, U. Ebels, S. O. Demokritov, J. Akerman, A. Deac, P. Pirro, C. Adelmann, A. Anane, A. V. Chumak, A. Hirohata, S. Mangin, S. O. Valenzuela, M. C. Onbaşlı, M. d'Aquino, G. Prenat, G. Finocchio, L. Lopez-Diaz, R. Chantrell, O. Chubykalo-Fesenko and P. Bortolotti, *Nat. Electron.*, 2020, **3**, 446–459.
5 Y. Liu, C. Zeng, J. Zhong, J. Ding, Z. M. Wang and Z. Liu, *Nano-Micro Lett.*, 2020, **12**, 93.
6 K. Elphick, W. Frost, M. Samiepour, T. Kubota, K. Takanashi, H. Sukegawa, S. Mitani and A. Hirohata, *Sci. Technol. Adv. Mater.*, 2021, **22**, 235–271.
7 C. J. Palmstrøm, *Prog. Cryst. Growth Charact. Mater.*, 2016, **62**, 371–397.
8 L. Bainsla and K. G. Suresh, *Appl. Phys. Rev.*, 2016, **3**, 031101.
9 T. Graf, C. Felser and S. S. P. Parkin, *Prog. Solid State Chem.*, 2011, **39**, 1–50.
10 F. Claudia and H. Burkard, *J. Phys. D: Appl. Phys.*, 2007, **40**, E01.
11 S. Chatterjee, S. Chatterjee, S. Giri and S. Majumdar, *J. Condens. Matter Phys.*, 2022, **34**, 013001.
12 S. E. Kulkova, S. V. Eremeev, T. Kakeshita and S. S. Kulkov, *Mater. Trans.*, 2006, **47**, 599–606.
13 I. Galanakis, P. H. Dederichs and N. Papanikolaou, *Phys. Rev. B: Condens. Matter Mater. Phys.*, 2002, **66**, 174429.
14 K. Ramesh Kumar, V. Chunchu and A. Thamizhavel, *J. Appl. Phys.*, 2013, **113**, 17E155.
15 A. Amirabadizadeh, S. A. Abbas Emami, Z. Nourbakhsh, S. M. Alavi Sadr and S. M. Baizaee, *J. Supercond. Novel Magn.*, 2017, **30**, 1035–1049.
16 I. Galanakis and E. Şaşıoğlu, *Appl. Phys. Lett.*, 2011, **99**, 052509.
17 A. K. Nayak, M. Nicklas, S. Chadov, P. Khuntia, C. Shekhar, A. Kalache, M. Baenitz, Y. Skourski, V. K. Guduru, A. Puri, U. Zeitler, J. M. D. Coey and C. Felser, *Nat. Mater.*, 2015, **14**, 679–684.
18 S. Kc, R. Mahat, S. Regmi, J. Y. Law, V. Franco, G. Mankey, W. H. Butler, A. Gupta and P. LeClair, *Acta Mater.*, 2022, **236**, 118112.
19 R. Chellakumar, T. S. D. Malar, A. N. Rawther and K. Ravichandran, *J. Supercond. Novel Magn.*, 2023, **36**, 547–557.
20 M. F. Tanzim, N. Fortunato, I. Samathrakis, R. Xie, I. Opahle, O. Gutfleisch and H. Zhang, *Adv. Funct. Mater.*, 2023, **33**, 2214967.
21 Y. Ji, W. Zhang, H. Zhang and W. Zhang, *New J. Phys.*, 2022, **24**, 053027.
22 S. Husain, A. Kumar, S. Akansel, P. Svedlindh and S. Chaudhary, *J. Magn. Magn. Mater.*, 2017, **442**, 288–294.
23 N. Nagaosa, J. Sinova, S. Onoda, A. H. MacDonald and N. P. Ong, *Rev. Mod. Phys.*, 2010, **82**, 1539–1592.
24 R. Karplus and J. M. Luttinger, *Phys. Rev.*, 1954, **95**, 1154–1160.
25 M. V. Berry, *Proc. R. Soc. London, Ser. A*, 1997, **392**, 45–57.
26 S. Roy, R. Singha, A. Ghosh, A. Pariari and P. Mandal, *Phys. Rev. B*, 2020, **102**, 085147.
27 J. Kudrnovský, V. Drchal and I. Turek, *Phys. Rev. B: Condens. Matter Mater. Phys.*, 2013, **88**, 014422.
28 M. Blinov, A. Aryal, S. Pandey, I. Dubenko, S. Talapatra, V. Prudnikov, E. Lähderanta, S. Stadler, V. Buchelnikov, V. Sokolovskiy, M. Zagrebin, A. Granovsky and N. Ali, *Phys. Rev. B*, 2020, **101**, 094423.
29 G. Xing, K. Masuda, T. Tadano and Y. Miura, *Acta Mater.*, 2024, **270**, 119856.
30 H.-L. Huang, J.-C. Tung and G.-Y. Guo, *Phys. Rev. B: Condens. Matter Mater. Phys.*, 2015, **91**, 134409.
31 G. Kresse and J. Hafner, *Phys. Rev. B: Condens. Matter Mater. Phys.*, 1993, **47**, 558–561.
32 G. Kresse and J. Hafner, *Phys. Rev. B: Condens. Matter Mater. Phys.*, 1994, **49**, 14251–14269.
33 G. Kresse, *J. Non-Cryst. Solids*, 1995, **192–193**, 222–229.
34 G. Kresse and D. Joubert, *Phys. Rev. B: Condens. Matter Mater. Phys.*, 1999, **59**, 1758–1775.
35 J. P. Perdew, K. Burke and M. Ernzerhof, *Phys. Rev. Lett.*, 1996, **77**, 3865–3868.
36 G. Pizzi, V. Vitale, R. Arita, S. Blügel, F. Freimuth, G. Géranton, M. Gibertini, D. Gresch, C. Johnson, T. Koretsune, J. Ibañez-Azpiroz, H. Lee, J.-M. Lihm, D. Marchand, A. Marrazzo, Y. Mokrousov, J. I. Mustafa,

Y. Nohara, Y. Nomura, L. Paulatto, S. Poncé, T. Ponweiser, J. Qiao, F. Thöle, S. S. Tsirkin, M. Wierzbowska, N. Marzari, D. Vanderbilt, I. Souza, A. A. Mostofi and J. R. Yates, *J. Condens. Matter Phys.*, 2020, **32**, 165902.
37 G.-Y. Guo, S. Murakami, T.-W. Chen and N. Nagaosa, Intrinsic Spin Hall Effect in Platinum: First-Principles Calculations, *Phys. Rev. Lett.*, 2008, **100**(9), 096401.
38 I. Galanakis, P. H. Dederichs and N. Papanikolaou, *Phys. Rev. B: Condens. Matter Mater. Phys.*, 2002, **66**, 174429.
39 J. Kubler, *Phys. B+C*, 1984, **127**, 257.
40 S. Kirklin, J. E. Saal, B. Meredig, A. Thompson, J. W. Doak, M. Aykol, S. Rühl and C. Wolverton, *npj Comput. Mater.*, 2015, **1**, 1.
41 X. Wang, J. R. Yates, I. Souza and D. Vanderbilt, *Phys. Rev. B: Condens. Matter Mater. Phys.*, 2006, **74**, 195118.
42 X. Wang, D. Vanderbilt, J. R. Yates and I. Souza, *Phys. Rev. B: Condens. Matter Mater. Phys.*, 2007, **76**, 195109.
43 H. R. Fuh and G. Y. Guo, *Phys. Rev. B: Condens. Matter Mater. Phys.*, 2011, **84**, 144427.
44 J. Noky, Y. Zhang, J. Gooth, C. Felser and Y. Sun, *npj Comput. Mater.*, 2020, **6**, 77.
45 P. Webster, *J. Phys. Chem. Solids*, 1971, **32**, 1221.
46 I. Galanakis, P. Dederichs and N. Papanikolaou, *Phys. Rev. B: Condens. Matter Mater. Phys.*, 2002, **66**, 174429.
47 E. Vilanova Vidal, G. Stryganyuk, H. Schneider, C. Felser and G. Jakob, *Appl. Phys. Lett.*, 2011, **99**, 132509.
48 J.-C. Tung and G.-Y. Guo, *New J. Phys.*, 2013, **15**, 033014.
49 J. Kübler and C. Felser, *Phys. Rev. B: Condens. Matter Mater. Phys.*, 2012, **85**, 012405.
50 M. Meinert, J.-M. Schmalhorst and G. Reiss, *J. Condens. Matter Phys.*, 2010, **23**, 036001.
51 Y. Han, Z. Chen, M. Kuang, Z. Liu, X. Wang and X. Wang, *Res. Phys.*, 2019, **12**, 435.
52 Y. Kudryavtsev, N. Uvarov, V. Iermolenko, I. Glavatskyy and J. Dubowik, *Acta Mater.*, 2012, **60**, 4780.
53 D. Xiao, Y. Yao, Z. Fang and Q. Niu, *Phys. Rev. Lett.*, 2006, **97**, 026603.